# Multistatic Radar Detection and Tracking of Drones

**Marc Schneebeli[1], Andreas Leuenberger[1], Urs Siegenthaler[2], Peter Wellig[2]**
[1]Palindrome Remote Sensing, Landquart
[2]armasuisse, Science and Technology, Thun
SWITZERLAND

marc.schneebeli@palindrome-rs.ch

## ABSTRACT

*The SAMURAI multistatic C-band radar system was originally developed as technology demonstrator in view of drone detection purposes in a range of up to 5 km. It consists of two receiving nodes operating with a digital beamforming antenna and a phased array transmitting node that illuminates the observation area with a fast scanning pattern. The radar signals are transmitted as linear frequency modulated (LFM) pulses, so that subsequent pulse compression enables range scanning with high resolution. More than 100 W of transmit power in a relatively narrow beam of about 4° results in high sensitivity, which is required for successful detection of objects with small radar cross sections. The system is usually set up in multistatic geometry, meaning that the nodes are distributed around the area of interest. The advantages of multistatic systems are their redundancy and the fact that zero Doppler conditions can be avoided. In addition, the geometry allows a more homogeneous distribution of the signal-to-noise ratio (SNR) over the observation area, in contrast to classical monostatic radars, where the SNR decreases in the fourth power to the radar distance. Radar systems with multiple receive nodes that are not collocated with the transmit node must be precisely aligned and calibrated for range so that a single target results in overlapping detections in the individual receive nodes. Geometric overlap is a prerequisite for successful track fusion algorithms, which are demonstrated for both simulated targets originating from two target generators and real targets originating from drones and vehicles. Geometric calibration using two non-collocated target simulators has been shown to provide the required accuracy for both range and directional calibration. The system has been employed in several field campaigns in both mountainous and urban environments for drone detection. Using real drones and simulated targets generated by two multistatic target generators, the detection capability of the system was evaluated and the implemented track generation was tested. Tracks generated from the two receiving nodes were fused in real-time to a single one allowing to continuously follow a drone even if track generation on one receiver is aborted.*

## 1.0   INTRODUCTION

SAMURAI is a bistatic C-band radar demonstrator, consisting of one transmit node and two receive nodes. It is being built by the Council for Scientific and Industrial Research, South Africa (CSIR) and was shipped to Switzerland and handed over to armasuisse in 2019. The radar's performance is described in [1] and an overview over the system can be found in [2]. In terms of signal processing, bistatic radars exhibit an increased complexity because synchronization between the transmit and the receive nodes is required but also more demanding than in monostatic systems. In addition, the levels of sophistication can be arbitrarily enhanced by increasing the number of receive nodes, by introducing coherent processing, by allowing the nodes to move and by introducing multiple transmit nodes [3]. Absolute calibration is a long-standing problem in radar science and remains an untackled issue even for monostatic radars. Monostatic radar calibration can be performed by using a reference target, whose monostatic Radar Cross Section (RCS) is well known, such as a sphere or a corner reflector. Alternatively, the transmit and receive characteristics of the radar are precisely measured such that the radar constant can be determined in high accuracy. Both methods become more demanding in the bistatic case. In general, the bistatic RCS is less well known than the monostatic RCS and it usually exhibits a high variability with respect to the scattering angle. While the

monostatic RCS of a metallic sphere depends only on the sphere diameter (if the sphere is small enough compared to the radar's wavelength), the bistatic RCS of the same sphere is different for every change in the scattering angle. Determining the radar constant of a bistatic system is also more demanding because of the physical separation of the transmitter / receiver nodes. Further complication arises from the fact that bistatic nodes are usually set-up on the ground with the main goal to detect close-to-ground targets. Such a geometry is prone to multipath contamination, since the transmitted and returning radar beams can be easily reflected on the ground surface. The ground surface not only induces multipath signals, it also contaminates the received signal spectrum in the zero-Doppler region with high signal amplitudes, which requires target velocities to be well above a certain threshold in order to appear out of the clutter region. The complications that arise with bistatic scattering are manifold. The bistatic RCS of a target is heavily influenced by the radar geometry, i.e., by the aspect angles of the target with respect to the transmit and receive nodes [4]. In general, bistatic RCS is also smaller than monostatic RCS as well as more variable because of the larger numbers of involved degrees of freedom. The lack in clutter statistics hence increases the difficulty to remove clutter from the scene of interest.

Why should a bistatic radar be employed despite all the mentioned difficulties? Certain drawbacks can turn into advantages for some specific applications. For example, the number of RX nodes increases the probability of a moving object to have a non-zero Doppler component in at least on TX-RX pair. From a military point of view, the fact that the RCS of stealth objects is minimized for the monostatic case increases the bistatic detection probability of such an object. Moreover, the SNR for certain TX-target-RX geometries can be advantageous compared to the monostatic case. And finally the target detection ambiguity introduced by several receivers helps to reduce false targets and increases the robustness of a target track.

## 1.1    System Description

SAMURAI consists of one transmit node, which generates a Linear Frequency Modulated (LFM) pulse by using a Software Defined Radio (SDR) as a signal generator. The signal from the SDR is split and fed into an amplitude weighting and phase shifting network before the individual signals are amplified and radiated over antenna array elements. Phase shifting and amplitude weighting lead to the formation of an antenna directional characteristic over which the LFM pulse is radiated towards the area of interest. Energy scattered towards one of the two receive nodes is received by 8 antenna elements, downconverted, digitized and sampled individually for every antenna element. The digital sample streams are multiplied by complex weights in order to select only data that originates from a certain direction. The weighted signals are passed through a matched filter to decompress the scattered LFM pulse. Signals exceeding a certain SNR are finally identified as targets and passed over for further processing. Targets are detected separately on the two independent nodes. Only the information on detected targets is then transferred to a common processing instance, where tracks are being built from subsequent detections. Tracks that originate from the same target and that appear on both of the two receivers are fused to a single track if certain criteria are being met.

## 2.0    BISTATIC RADAR FUNDAMENTALS

This section provides an overview of fundamental bistatic radar principles, such that the further reading is simplified. The section gives definitions of the bistatic geometry and proceeds to the radar range equation. It considers noise aspects and bistatic Doppler relations as well as signal processing aspects.
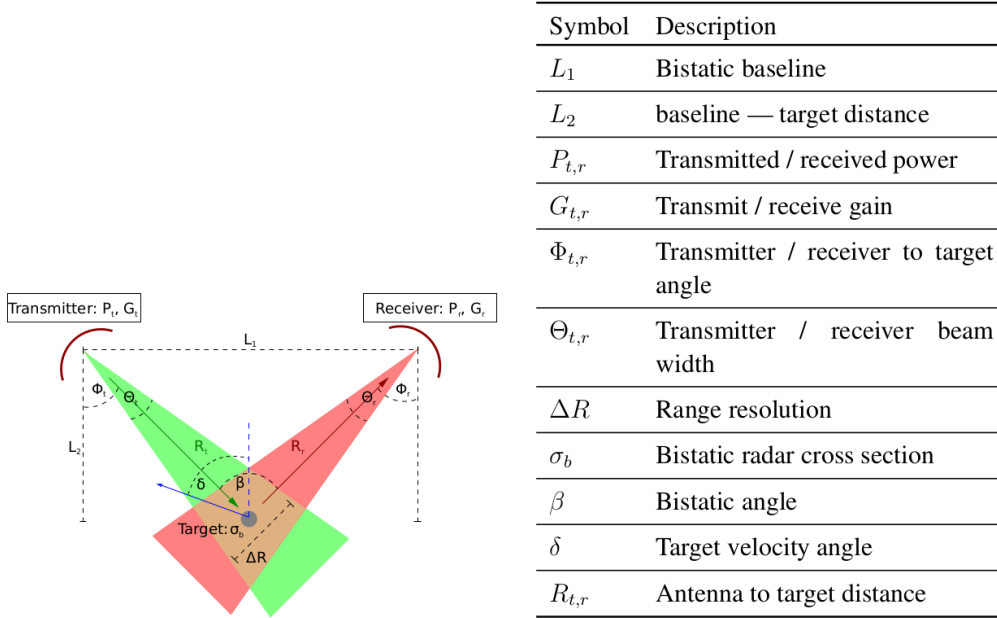
## 2.1    Radar Range Equation

The basic bistatic radar geometry is depicted in Figure 1. The table given therein introduces the nomenclature used in the following.

According to and without any further derivation, the point target bistatic radar equation can be written as

$$\frac{P_r}{P_t} = \frac{G_t G_r \lambda^2}{(4\pi)^3 R_t^2 R_r^2} \sigma_b(\beta) \tag{1}$$

where receiver noise, processing aspects, losses and propagation effects have been omitted. The definition of the variables can be found in Figure 1. In addition to this table, $\lambda$ denotes the wavelength of the radar's carrier signal.



| Symbol | Description |
|---|---|
| $L_1$ | Bistatic baseline |
| $L_2$ | baseline — target distance |
| $P_{t,r}$ | Transmitted / received power |
| $G_{t,r}$ | Transmit / receive gain |
| $\Phi_{t,r}$ | Transmitter / receiver to target angle |
| $\Theta_{t,r}$ | Transmitter / receiver beam width |
| $\Delta R$ | Range resolution |
| $\sigma_b$ | Bistatic radar cross section |
| $\beta$ | Bistatic angle |
| $\delta$ | Target velocity angle |
| $R_{t,r}$ | Antenna to target distance |

**Figure 1: Sketch of the bistatic radar geometry with the respective nomenclature definition of basic bistatic variables.**

The quantity the radar finally delivers is usually related to the Signal-to-Noise (SNR) defined as

$$\text{SNR} = \frac{P_r}{P_n} = \frac{P_r}{k_B T_s B_n} \tag{2}$$

where $P_n$ is the receiver noise power, $k_B$ the Boltzmann constant, $T_s$ the receiver noise temperature and $B_n$ the noise bandwidth of the receiver's pre-detection filter.

Equation 1 is valid for a perfect system. Deviations from perfectness occur from pointing errors, multipath effects, diffraction and refraction (i.e., pattern propagation) as well as from unaccounted losses. These effects can be summed up into transmitting and receiving pattern propagation factors, $F_{r,t} \leq 1$, and loss terms $L_{r,t} \geq 1$ which include atmospheric losses. By combining Equations 1 and 2 and taking into account propagation effects and losses, the SNR induced by a single point target in a radar receiver can be written as

$$\frac{P_r}{P_n} = \frac{P_t G_t G_r \lambda^2 F_t^2 F_r^2 \sigma_b(\beta)}{k_B T_s B_n (4\pi)^3 R_t^2 R_r^2} \tag{3}$$

Since $F_{r,t}$ are customarily defined by the strength of the theoretical electric field at the receiving antenna with respect to a actual electric field, they appear squared in Equation 3.

## 2.2 Bistatic Radar Cross Section

The bistatic RCS $\sigma_b(\beta)$ defines how much power $P_{rer}$ intercepted by the target is re-radiated toward the receive antenna. If the target is illuminated by the incident power density $S^i$ and the angle between $S^i$ and $P_{rer}$ is the bistatic angle $\beta$, the RCS is defined as

$$P_{rer} = \sigma(\beta) S^i \tag{4}$$

The re-radiated power results at a distance $R$ from the target in scattered power density

$$S^s = \frac{P_{rer}}{4\pi R^2} \tag{5}$$

and hence the definition of the RCS is alternatively obtained by combining Equations 4 and 5 as

$$\sigma_b(\beta) = 4\pi R^2 \frac{S^s(\Phi_r)}{S^i(\Phi_t)} \tag{6}$$

where $R$ indicates the range at which $S^i$ is measured, $\Phi_{r,t}$ indicate the propagation directions of the power densities and $\beta = \Phi_r + \Phi_t$.

## 2.3 Bistatic Radar Doppler Shift

In a monostatic configuration, the return signal scattered at a target located at range $R$ with velocity $v_r = dR/dt$ assumes the well known frequency shift

$$f_D = \frac{2v_r}{\lambda} \tag{7}$$

The corresponding Doppler frequency shift for a bistatic radar is

$$f_D = \frac{1}{\lambda}\left[\frac{d}{dt}(R_t + R_r)\right] = \frac{1}{\lambda}\left[\frac{dR_t}{dt} + \frac{dR_r}{dt}\right] \tag{8}$$

It is assumed that the receiver and the transmitter are stationary and that the target moves with a velocity $v$ in the direction of the blue arrow in Figure 1. The time derivative of the first term in Equation 8 is the rate of change of the transmitter to target path, i.e., the projection of the velocity vector onto the $R_t$ vector:

$$\frac{dR_t}{dt} = v\cos\left(\delta - \frac{\beta}{2}\right) \tag{9}$$

where the dashed blue line in Figure 1 assumes an angle of $\beta/2$ and $\delta$ is the angle between the target velocity vector and the dashed blue line. Likewise, the rate of change of the target to receiver path is evaluated as:

$$\frac{dR_r}{dt} = v\cos\left(\delta + \frac{\beta}{2}\right) \tag{10}$$

Combining Equations 8, 9 and 10 yields

$$f_D = \frac{2v}{\lambda}\cos(\delta)\cos\left(\frac{\beta}{2}\right) \tag{11}$$

## 3.0 GENERATION OF BISTATIC RADAR TARGETS

A Radar Target Simulator (RTS) is a system that is able to generate an artificial radar target at a predefined distance and with predefined Doppler shift and radar cross section (RCS). For a monostatic radar, the RTS receives the pulses emitted by the radar, modulates them and sends them back to the radar with a certain time delay, which corresponds to the distance at which the artificial target is supposed to appear on the radar screen. The frequency shift applied to the returned pulse is given by Equation 7. The time delay $\Delta t$ that needs to be applied to the pulses that are sent back to the monostatic radar is given by

$$\Delta t = \frac{2(R_v - R_r)}{c} \tag{12}$$

where $R_v$ is the distance of the virtual target to the radar and $R_r$ is the distance between the radar and the RTS.

For a given RCS $\sigma_b$ the artificial target should have, only a certain fraction $F$ of the incoming pulse power is being sent back to the radar. This fraction can be determined with Friis' transmission equation and reads:

$$F = \frac{4\pi R_r^4 \sigma_b}{G_{RTS}^2 \lambda^2 R_v^4} \tag{13}$$

$G_{RTS}$ is the antenna gain of the RTS, assuming that the receive and transmit antennas are equal.

In the bistatic case, the above equations need to be slightly adjusted. Equation 13 needs to be rewritten to:

$$F = \frac{4\pi R_{t,RTS}^2 R_{r,RTS}^2 \sigma_b}{G_{RTS}^2 \lambda^2 R_{t,v}^2 R_{r,v}^2} \tag{14}$$

where $R_{t,v}$ is the distance from the transmitter to the virtual target, $R_{r,v}$ is the distance from the virtual target to the receiver, $R_{t,RTS}$ is the distance from the transmitter to the RTS and $R_{r,RTS}$ is the distance from the RTS to the receiver.

It needs to be noted that the above equations do not take into account multipath effects, which may hamper the accuracy of transponder based calibrations, as detailed in [6]. However, calibration targets like trihedral reflectors are also prone to multipath effects. In contrast to such real targets the advantages in using virtual targets are manifold: Due to the application of a Doppler shift, the target can be shifted out of the clutter contaminated zero-Doppler region. In addition, RCS and range distances can be freely selected and the bistatic RCS of traditional calibration objects impose further difficulties for the calibration of non-monstatic radars.

Palindrome Remote Sensing has developed a polarimetric dual-channel RTS system which was adapted to multistatic geometries. The Palindrome RTS is able to generate multiple virtual point target with a specific Doppler shift and RCS by receiving the SAMURAI's LFM pulse and transmitting it back towards the two radar RX nodes with individual time delays and Doppler shifts. Generated targets can be static or moving along trajectories. A built-in feedback loop ensures that the RCS of the virtual target remains stable during the test. The two employed system are depicted in Figure 2.

*Image unavailable*

**Figure 2: The two Palindrome radar target simulators that were employed for the generation of electronic calibration targets.**

## 4.0 MONOSTATIC MEASUREMENTS

The receive and transmit nodes were deployed in April 2020 in a quasi-monostatic configuration. The target simulator was deployed in a distance of 550 m to the radar nodes. The altitude of all the nodes was approximately 550 m above sea level (asl). A map of the setup and a photo of the deployed nodes is shown on the lefthand side of Figure 3.
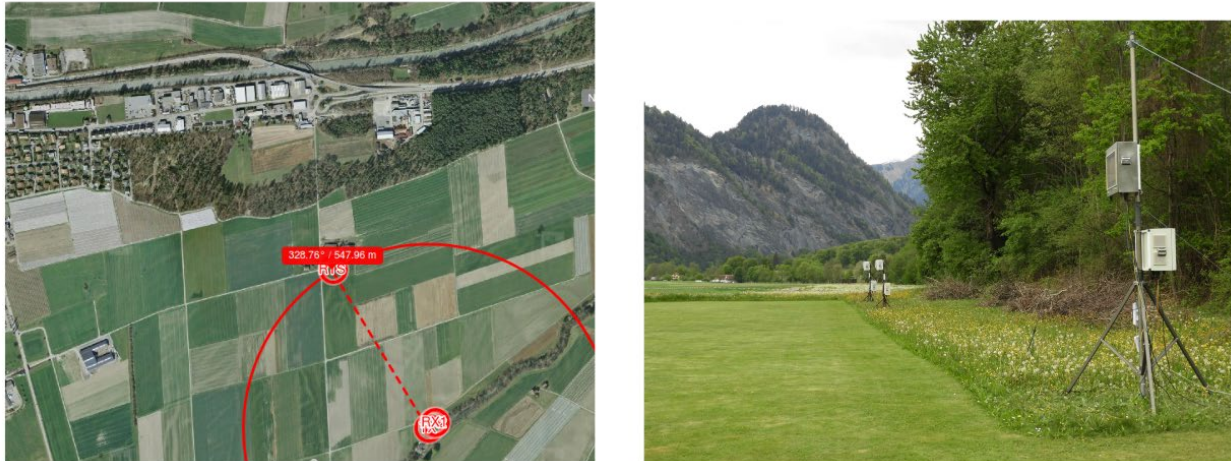


**Figure 3: Left: Aerial map showing the deployment of the SAMURAI nodes and the RTS. Right: Photo of the SAMURAI nodes with the transmitter in the foreground and the receivers in the background.**

### 4.1 Drone Measurements

A DJI Phantom 4 drone with real-time kinematics (RTK) high-precision GPS was used as a real test target. The RTK option provides corrected drone location information with an accuracy in the range of few centimeters.

Figure 4 shows the detected southward flying drone (marked by the green square). The detections are cumulated over a time period of 6 s. Geometrical (i.e., range and azimuthal) corrections were applied at a later stage in the processing and hence an offset in range and direction between the two receive nodes is clearly visible. The area of the green square is shown for four detection parameters in Figure 5, i.e., detection age on the left panel, received power level in the middle panel and Doppler frequency shift on the right panel. The average value for the power level is -15 dBm and for the Doppler frequency shift a value of 480 Hz (approx. 12.5 m/s) for all detections was found.

### 4.2 Drone Flight Analysis

The radar detections of the DJI drone were compared to the GPS-measured trajectories of the drone. The GPS trajectory of a 5-min long flight together with uncorrected RN1 and RN2 detections are depicted on the left panel of Figure 6. Node synchronization and alignment difficulties lead to relatively large deviations between the GPS trajectory and the drone detections. However, these deviations can be accurately determined by means of virtually generated targets, as detailed in [7]. In the post-processing, the receive nodes azimuthal pointing as well as their range offsets are deduced from the virtual target measurements and corresponding corrections are applied to the detections. The post-processed corrected image is shown in on the right panel of Figure 6.

It is seen that the correction for RN1 is not yet perfect. It is speculated that the reason behind the persisting offset is a slight angular movement of RN2 after the azimuthal offset has been determined with the target generator.
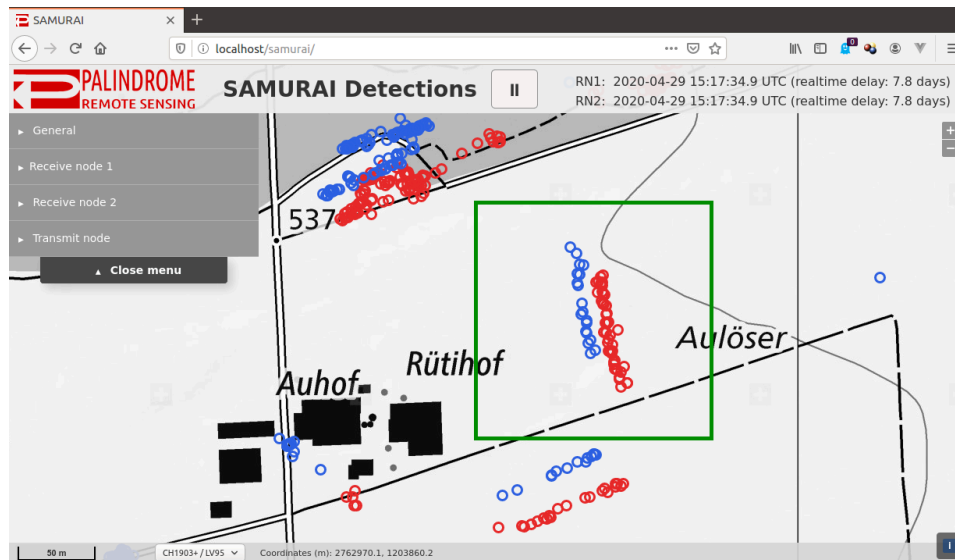


**Figure 4: The green square shows the detections of the drone during 6 s. The detections of receive node 1 are shown in red, the detections of receive node 2 in blue.**
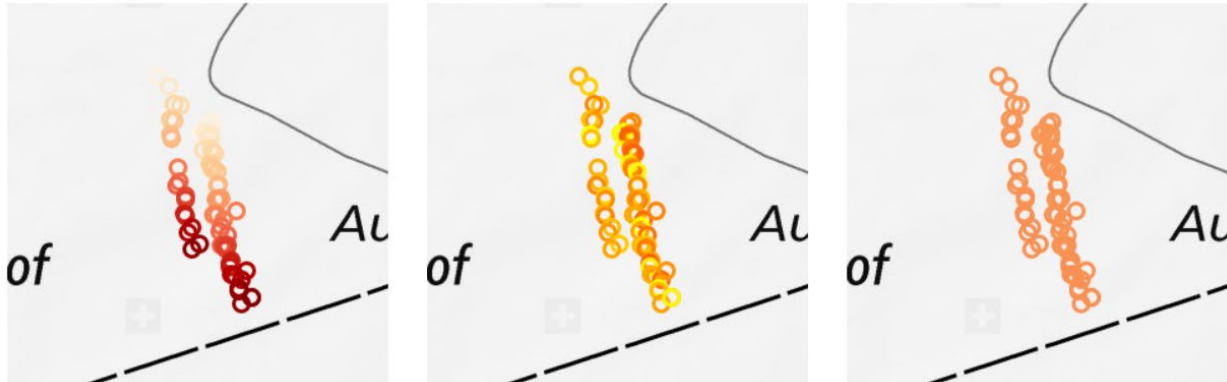


**Figure 5: The three images show the green area indicated by Fig. 4. and show the detections of both receive nodes by age (left), by power level (middle) and by Doppler frequency (right).**
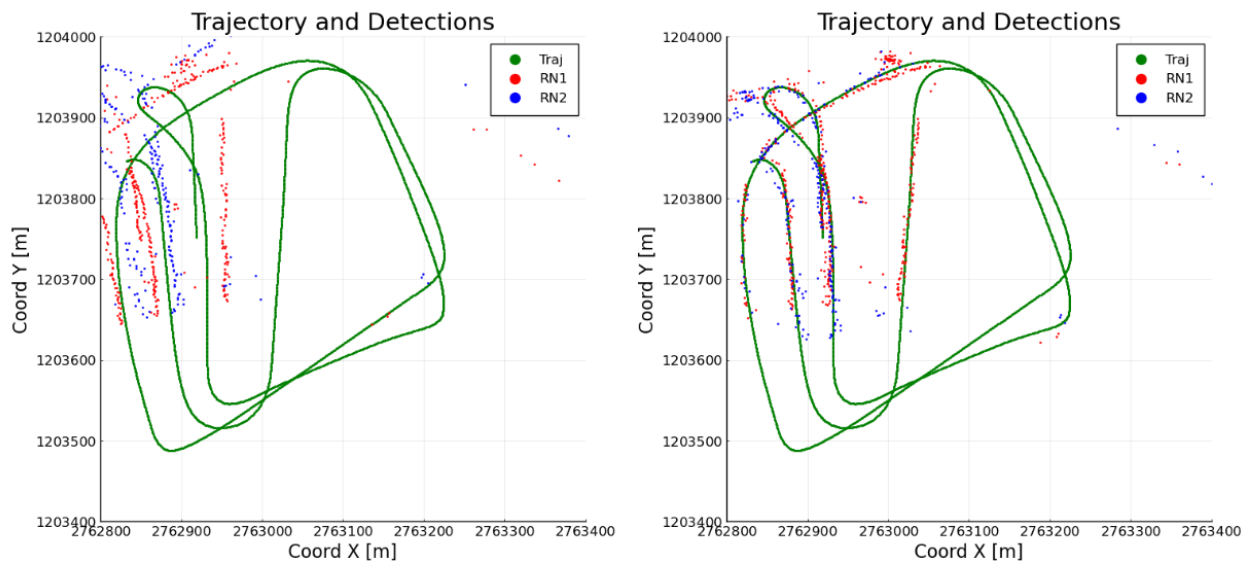
**Figure 6: Left: Drone trajectory from the onboard GPS together with the uncorrected SAMURAI detections from RN1 and RN2. Right: Same as on the left but with geometrical range and azimuth correction applied.**

## 4.3 Virtual Target Measurements

### 4.3.1 Static Targets

Static virtual targets were generated with the RTS at 4 and 5 km distance to the radar, as shown on the left panel of Figure 7. An angular offset is observed which indicates that the boresight angle of one or both of the receive nodes is not properly determined. The one-way distance offsets of RN1 and RN2 were determined to a value of 120 m and 150 m, respectively.

### 4.3.2 Moving Targets

A virtual target moving from 5 to 4 km distance to the radar with an RCS of 10 m² was generated. The target speed was set to 10 m/s. However, in order to be able to properly filter the detections, a Doppler speed of 800 Hz was assigned to the target. This Doppler speed does not correspond to the actual speed of the target but its application facilitated the target display, since the display processor allows the filtering of targets by applying a Doppler criterion. The moving target was generated in order to test some features of the visualization software and the capabilities of the RTS. An example of a moving virtual target is shown on the right panel of Figure 7. For upcoming experiments, the RTS will generate numerical values of its virtual target trajectories, such that drone trajectories obtained from the radar can be directly compared to the virtual target trajectories in order to obtain geometrical correction parameters automatically and in quasi real-time.
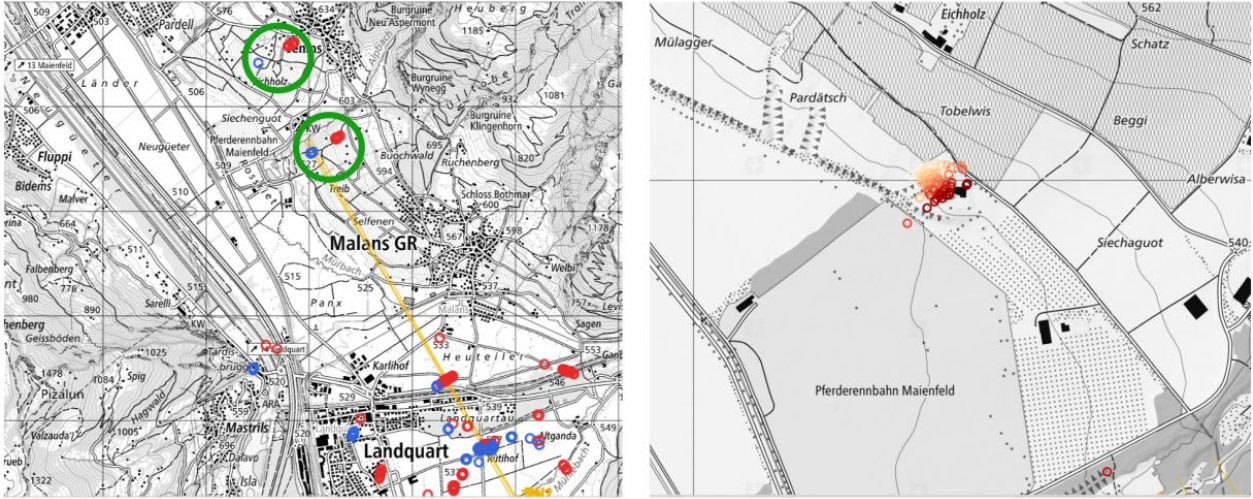
**Figure 7: Left: Virtual target at 4 and 5 km distance to the radar. The virtual targets are marked with a green circle. Right: Moving virtual target with a target speed of 10 m/s . The color coding (from white to red) shows the age of the detections, with dark red indicating the most actual ones.**

## 4.4 Radar Calibration

The goal of the RTS is to loop back the receive signal such that the power of the transmit signal has a well-defined ratio to the power of the receive signal. This ratio is called RTS factor $K$ and is defined as

$$K = \frac{p_t}{p_r} \tag{15}$$

with $p_{t,r}$ being the RTS transmitted and received power, respectively. The RTS factor $K$ is calculated by the RTS software dependent on the location of the radar and the radar cross section (RCS) $\sigma$ of the simulated target. Any effects inside the RTS that lead to a change in $K$ are being compensated, with frequency and temperature dependence being the most dominant effects of the hardware components.

From the power ratio $K$ behind the RTS antenna defined in Equation 15 the RCS $\sigma$ of a virtual target located at a distance $r_t$ to the radar is calculated as

$$\sigma_b(\beta) = \frac{K r_t 4 G_{rts}^2 \lambda^2}{r_r^4 4\pi} \tag{16}$$

where $r_r$ is the distance from the RTS to the radar and $G_{rts}$ is the antenna gain of the RTS.

According to [6], the point target bistatic radar equation can be written as

$$\frac{P_r}{P_t} = \frac{G_t G_r \lambda^2}{(4\pi)^3 R_t^2 R_r^2} \sigma_b(\beta) \tag{17}$$

where receiver noise, processing aspects, losses and propagation effects have been omitted. In the above equation, $G_{t,r}$ denote the antenna gain of the transmit (t) and receive (r) antenna, $P_{r,t}$ the transmitted and received power, $R_{t,r}$ the range to the target from the transmitter and receiver, respectively, $\lambda$ the wavelength, $\sigma_b(\beta)$ and the bistatic radar cross section as a function of the bistatic angle $\beta$.

The SAMURAI radar measures the received and digitized power $P_{r,dig}$ associated with every detected target. The goal of the calibration procedure is to relate $P_{r,dig}$ to the target's $\sigma_b(\beta)$. To do so, Equation 17 can be rewritten and simplified to

$$\sigma_b(\beta) = CP_{r,dig}R_t^2 R_r^2 \tag{18}$$

The constant $C$ is determined with the RTS by generating a virtual target with a defined RCS at a defined range, as it is shown on the lefthand side of Figure 7. A virtual target was generated at a distance of 4 km to the radar with different RCS ranging from 0.05 m² to 0.001 m².
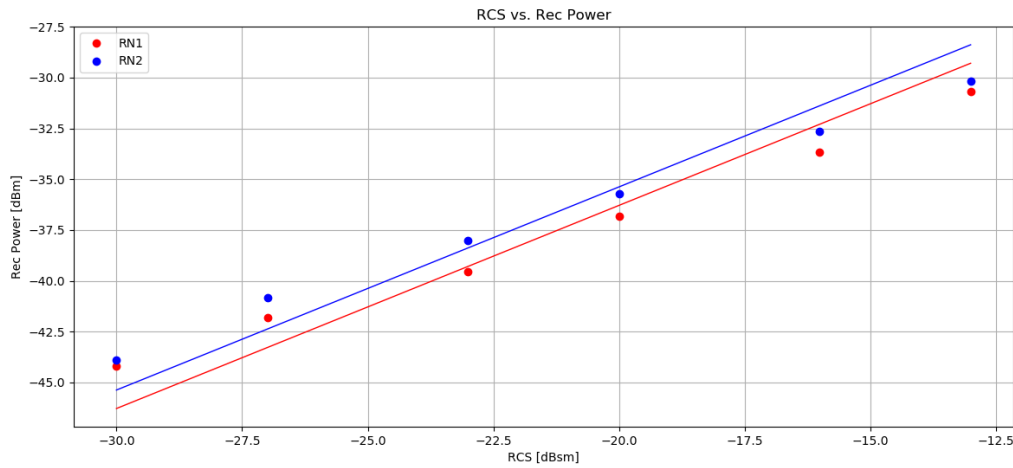


**Figure 8: Received power vs. RCS of the virtual target.**

The power level $P_{r,dig}$ detected by the radar as a function of the RCS is shown in Figure 8. A Doppler speed of 800 Hz was applied to the virtual target such that it could be filtered out from possible clutter targets that contaminated the surroundings of the target of interest.

The measurements shown in Figure 8 were approximated with a linear fit. The results are given below:

$$\sigma_b(\beta) = P_{r1,dig} + 20\log_{10}(R_r) + 20\log_{10}(R_t) - 127.8 \tag{19}$$

$$\sigma_b(\beta) = P_{r1,dig} + 20\log_{10}(R_r) + 20\log_{10}(R_t) - 128.7 \tag{20}$$

For the above equations, $P_{r,dig}$ is in [dBm], $R_{t,r}$ in [m] and $\sigma_b(\beta)$ in [dBm²].

It needs to be noted that for the detection of the generated calibration targets a SNR threshold of 20 dB was selected for targets fulfilling $\sigma_b(\beta) \geq 0.02m^2$ and an SNR threshold of 10 dB was selected for targets fulfilling $\sigma_b(\beta) \leq 0.01m^2$. With an SNR threshold of 20 dB, targets with an RCS $\sigma_b(\beta) \leq 0.001m^2$ could not be detected anymore at a distance of 4 km.

The distance of the drone to the radar in the detections displayed in Figure 5 was around 602 m. Using Equation 19 for the calculation of the RCS together with the drone measurements displayed in Figure 5, the drone RCS can be estimated to a value of approximately $-30dBm^2$. The problem with Equation 19 is that slight changes in the distance or the received power lead to very different RCS values. This is due to the assumption of a constant noise contribution that eventually needs to be adapted for more sophisticated RCS measurements. It is also recommended to use a large ensemble of detections for the calculation of a drone

RCS. The RCS of a DJI Phantom 2 drone, which has geometrical similarities to the model used during our tests, was measured in an anechoic chamber to a value of $-27\text{dBm}^2$ [8], while radar based RCS measurements of a DJI Phantom 4 at 8.75 GHz led to values of up to $-10\text{dBm}^2$ and an average of $-16\text{dBm}^2$ [9].

## 5.0 MULTISTATIC DRONE MEASUREMENTS

### 5.1 Experimental Set-Up

In several field campaigns conducted between 2019 and 2022, SAMURAI's capability for multistatic drone detection was exploited. The campaigns together with a description of the test procedures were documented in [8,11]. From the many drone flights that were conducted during these campaigns, the one depicted in Figure 10 shows particularly well the advantages and drawbacks of a multistatic geometry.

The DJI Phantom 4 drone was following a circular trajectory with a diameter of 400 m, a speed of 10 m/s at an altitude of 40 m above ground. The center of the flown trajectory together with the position of the SAMURAI nodes is shown in Figure 9.
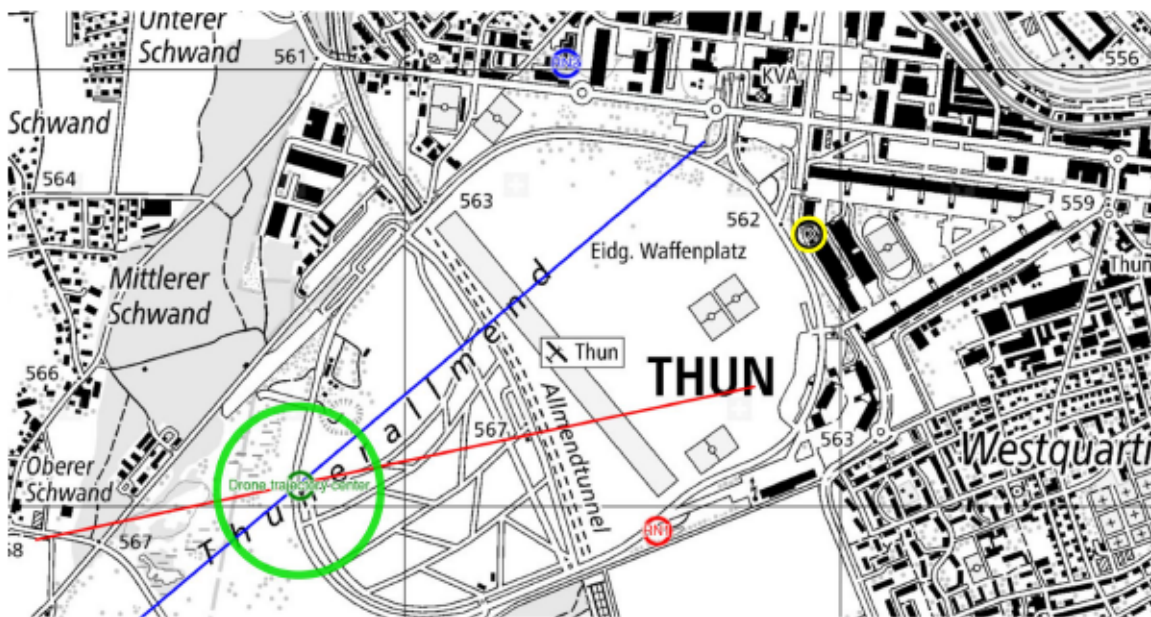


Figure 9: Multistatic node setup with receive node 1 (red), receive node 2 (blue), transmit node (yellow) and the drone trajectory (green). The red and blue lines indicate the zero Doppler direction of the respectively colored nodes.

The most prominent feature in Figure 10(a) is the trajectory offset of the detections from RN1. This offset is corrected with the RTS as already discussed and the post processing result is seen in Fig. 10b. Detection gaps are found in the zero Doppler directions indicated in Figure 9. These directions are derived from the bistatic Doppler shift equation given in Equation 8.

The target exhibits no Doppler shift if $\delta=90°$ and directions fulfilling this condition are drawn in Figure 9. The fact that the zero-Doppler induced detection gaps occur at different directions for the two receivers is one of the main advantages of the bistatic geometry.
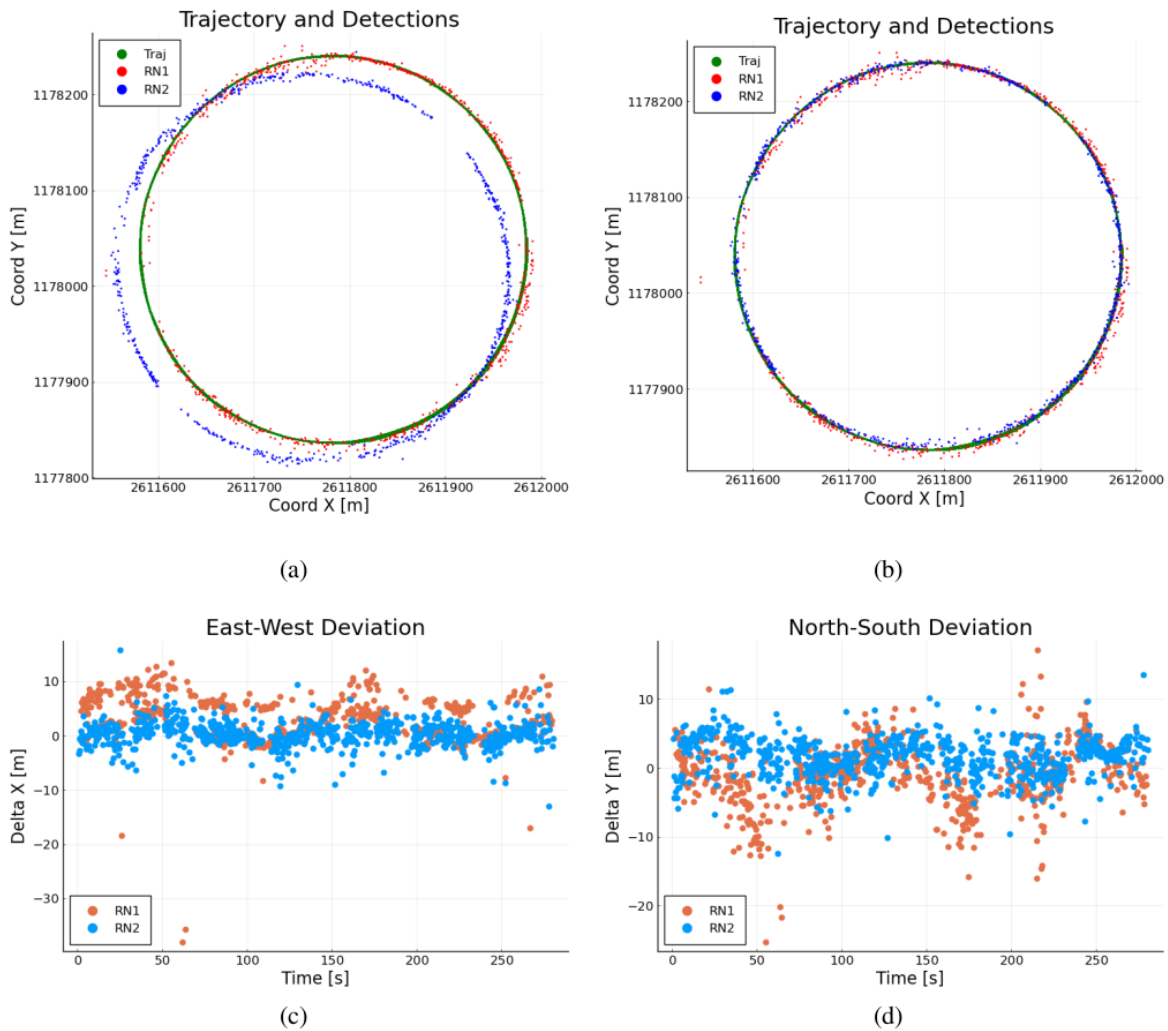
Figure 10: (a) Drone flight pattern and the RN1 and RN2 detections before any correction has been applied. (b) Same as in (a) but with applied range and azimuthal corrections. (c) East-West deviation of the detections with respect to the drone's GPS after the correction. (d) Same as in (c) but for the North-South deviation.

Figure 10c and 10d show an evaluation of the East-West and North-South deviations of the corrected radar detections with respect to the drone's GPS position. Still a slight offset of maximally 10 m is present for RN1 detections. If angular and range biases are fully removed as for the RN2 detections, the system exhibits an accuracy on the order of 5 m.

## 5.2    Geometrical Calibration with Target Simulators

Node synchronization as well as node alignment were identified as one of the major challenges for successfully employing multistatic radars for drone detection purposes. On one hand, the zero-range gate, i.e., the range gate at which the multistatic range $R_m$, is zero, tends to be more difficult to evaluate since the transmitter is not collocated to the receiver. The multistatic range $R_m$ is hereby defined as

$$R_m = R_{t,T} + R_{r,T} - D_{r,t} \qquad (21)$$

where $R_{t,T}$ is the distance from the transmitter (Tx) to the target, $R_{r,R}$ is the distance from the target to the receiver (Rx) and $D_{t,r}$ is the distance between Rx and Tx.

On the other hand, every node has an individual boresight direction that needs to be precisely known if geo-referenced detections are required. In the case of a multi-receiver geometry, overlapping detections and tracks that originate from a single target also need to undergo a fusion process: Detections that are generated by an individual Rx node need to be unambiguously allocated to the original target. In case of multiple Rx nodes, an individual target can generate detections on every Rx node, which may lead to ambiguities. A prerequisite of such a fusion process is the exact overlap of the coordinates of detections that stem from a single target.

Geometrical calibration has been achieved by employing two RTS systems that were capable to generate point targets and trajectories in two different directions, as shown on the left panel of Figure 11. Since the location the generated virtual targets is very precise, they can serve as reference for the exact determination of the receive node's boresight directions and zero range gate.

## 5.3    Track Generation and Fusion

### 5.3.1    Track Generation

Track generation is based on time series of detections. After a new track is being generated in a first stage, an extrapolation of an already existing track is performed subsequently. A new track is started if the distance between two detections from different coherent processing intervals (CPI) is smaller than a maximal distance, which is calculated as the product of the configured maximal velocity a moving object can assume times the time difference of the two detections.

The maximal time difference between the timestamp of two detections is limited. The limitation depends on the number of transmit scan directions. As a further criterion, the two detections are not allowed to be part of an already existing track. An algorithm described in [10] decides if a new track point is appended to an already existing track. Likewise, the algorithm decides when tracks are aborted if detections are missing. The whole track generation process has been tested with virtually generated trajectories that originated from the two already described target simulator systems. Such virtual radar trajectories can be seen in Figure 11. In this Figure, every target simulator generates one virtual trajectory per receive node. For geometrical reasons, two trajectories that originate from one RTS overlap only on one point, which is the location of the RTS itself.

### 5.3.2    Track Fusion

In the first part of the track fusion process, the new tracks from both receive nodes are analyzed and overlapping tracks that could potentially be fused are identified. The second part of the algorithm deals with the extension of an already existing fusion track. Once a fusion track exists, it is tested periodically if it is still valid according to a list of scenarios that are described in [10]. Track fusion can be tested with virtually generated trajectories if the radar is set up in a monostatic geometry. This is has been done extensively in field experiments described in . A track fusion example with a real drone targets is shown in Figure 11. In this Figure, a DJI phantom 4 drone was flying on a circular trajectory and detections of two receive nodes were fused in real-time. Thanks to the fusion process, a coherent and uninterrupted track could be generated, despite the fact that several zero-Doppler conditions were fulfilled along the track. The multi-static geometry however ensured that these conditions appeared at different locations along the track for the two receive nodes, such detections of at least one receiver were continuously obtained.
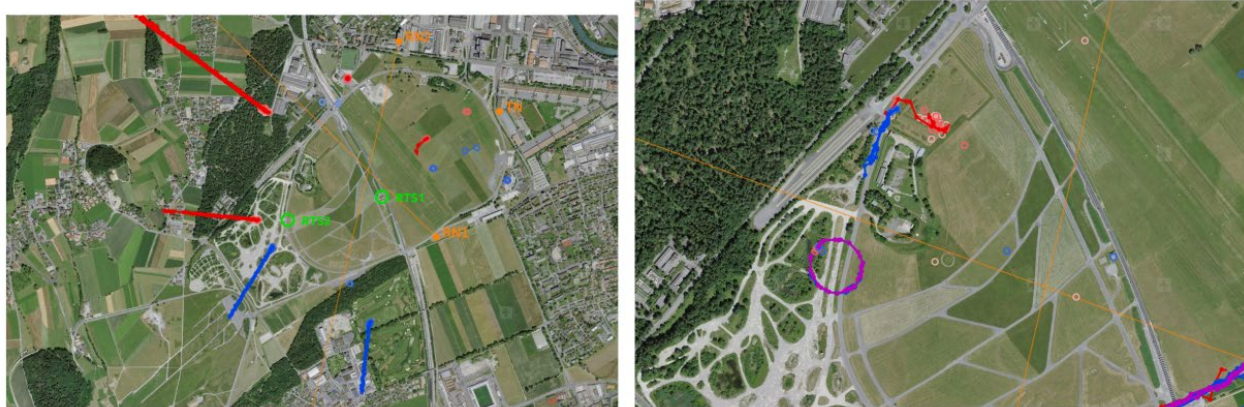
**Figure 11: Left: Virtual target trajectories generated with two target simulator systems. Right: Fused track (purple color) of a DJI Phantom 4 drone.**

## 6.0   CONCLUSIONS

Despite technical challenges in node synchronization, geometrical calibration and data transfer between distributed nodes, it could be shown that drone detection with multistatic radar systems is feasible. In a series of field experiments, the radar system SAMURAI was calibrated with two target simulators, track generation and track fusion was implemented and tested with virtually generated trajectories and finally, the applicability towards real-time detection of small aerial vehicles has been demonstrated. Overlapping drone trajectories were obtained after the radar has been precisely calibrated with with electronically generated targets. This was a prerequisite for a subsequent merging process of trajectories that were generated on individual receive nodes that originate from one single moving object. Trajectory interruptions caused by zero Doppler conditions could be overcome thanks to the multi-receiver geometry. Multistatic radar configurations were found to have high potential for future commercial systems in terms of drone detection and tracking in complex environments. However, time and phase synchronization between nodes along with precise geometric alignment is critical for all aspects of signal processing.

## 7.0   REFERENCES

[1]   V. Janse van Rensburg, W. A. J. Nel, J. E. Cilliers, U. Böniger, U. Siegenthaler, and P. Wellig, "High level performance model and performance comparison for multistatic radar system design," in IEEE Radar Conference. Philadelphia, USA: IEEE, 2015.

[2]   U. Böniger, P. Wellig, W. A. Nel, J. E. Cilliers, K. C., K. Kloke, V. Janse van Rensburg, L. Wabeke, and S. Govender, "WYSIWYG or the more you see the better you get? Towards a multistatic C-band radar system," in NATO STO Specialists' Meeting, 2015.

[3]   H. Griffiths, Novel Radar Techniques and Applications. London, UK: Scitech publishing, 2018, vol. 2: Waveform Diversity and Cognitive Radar, and Target Tracking and Data Fusion, ch. 8: The concept of the intelligent radar network.

[4]   H. Griffiths and R. Palamà, Novel Radar Techniques and Applications. London, UK: Scitech publishing, 2018, vol. 2: Waveform Diversity and Cognitive Radar, and Target Tracking and Data Fusion, ch. 6: Clutter diversity.

[5]   F. T. Ulaby and D. G. Long, Microwave Radar and Radiometric Remote Sensing. Ann Arbor, US: The University of Michigan Press, 2014, ch. 5: Radar scattering.

[6]    B. J. Döring, J. Reimann, S. Raab, M. Jirousek, D. Rudolf, and M. Schwerdt, "The three-transponder method: A novel method for accurate transponder RCS calibration." Prog. Electromagnetics Res. B, vol. 61, pp. 291 – 315, 2014.

[7]    M. Schneebeli, A. Leuenberger, U. Siegenthaler, and P. Wellig, "Testing a multistatic C-band radar with a target simulator," in International Radar Symposium 2020. Warsaw, Poland: IEEE, 2020.

[8]    L. O. Wabeke, S. Govender, J. E. Cilliers, K. Kloke, R. Philip, and W. A. J. Nel, "SAMURAI multistatic radar technology demonstrator progress report," Council of Scientific and Industrial Research CSIR, Pretoria, South Africa, Tech. Rep. 5865-MSRR-00005-RPT Rev 2, 2017, order 8003515352.

[9]    Á. Duque de Quevedo, F. Ibañez Urzaiz, J. Gismero Menoyo, and A. Asensio López, "Drone detection and RCS measurements with ubiquitous Radar," in International Conference on Radar 2018, 2018.

[10]   M. Schneebeli, A. Leuenberger, U. Siegenthaler, and P. Wellig, "Multistatic radar applications in combination with two target simulators," in 2023 24th International Radar Symposium (IRS), 2023, pp. 1–10.